Optics Letters

Generating a multi-mode vortex beam based on spoof surface plasmon polaritons

Juan-Feng Zhu,[1] Chao-Hai Du,[1,*] Zi-Wen Zhang,[2] and Fan-Hong Li[2]

[1]Center for Carbon-Based Electronics and State Key Laboratory of Advanced Optical Communication Systems and Networks, School of Electronics, Peking University, Beijing 100871, China
[2]State Key Laboratory of Advanced Optical Communication Systems and Networks, School of Electronics, Peking University, Beijing 100871, China
*Corresponding author: duchaohai@pku.edu.cn

Received 1 June 2022; revised 22 July 2022; accepted 4 August 2022; posted 4 August 2022; published 26 August 2022

The vortex beam provides a promising alternative for next-generation wireless communication, but it is a long-standing challenge to generate a multi-mode and robust vortex beam. In this Letter, a multi-mode vortex beam emitter is introduced and experimentally verified based on spoof surface plasmon polaritons (SSPP). The SSPP on a helical grating carries multi-mode orbital angular momentum and can be converted into a high-purity vortex beam via the diffraction of a ring array. The operation frequency and topological charge are determined by that of the SSPP. This emitter can achieve the function of beam-scanning in each radiation band. The beam-scanning and vortex characteristics are experimentally verified. The designed emitter is compact and robust, and we are confident that this work will have great application prospects in communication systems.

https://doi.org/10.1364/OL.465695

The vortex beam, which carries the orbital angular momentum (OAM) mode, has attracted much interest since its first discovery [1–5]. In particular, the vortex beam has unbounded orthogonal eigenstates and can be used to multiplex communication channels without increasing the cost of bandwidth [6]. To further explore its underlying physical characteristics and potential applications, generating vortex beams has attracted considerable attention from both science and engineering. To date, there are several ways to achieve it. Initially, the spiral phase plate is widely used to convert the incoming wave into a vortex beam [7]. The antenna array and metasurface are flexible to produce a vortex beam by arranging the angular phase distribution [8–10]. Additionally, the ring resonators are used to produce the vortex beam at resonant frequencies [11]. However, there are still several limitations to generating non-resonant multi-mode vortex beams.

The spoof surface plasmon polariton (SSPP) is also a desirable candidate for generating the vortex beam as its physical characteristics can be manipulated by structural parameters [12–14]. The looped SSPP leaky waveguide has been proposed to achieve an integrated vortex beam emitter [15,16]. However, it relies on the resonant effect of the structure and the bandwidth is strictly limited. The helical structure is an ideal candidate to generate a vortex beam as the azimuthal physical structure can modulate the wavefront. For example, the vortex beam from a helical system is reported in our previous work [17–19]. It is worth pointing out that these emitters are irrelevant to the SSPP and are mainly manipulated by the diffraction order. Encouragingly, the SSPP on the helical grating carries the OAM mode, providing an excellent solution to generate a vortex beam [20,21]. In this Letter, a tunable multi-mode vortex beam emitter based on SSPP is introduced. The SSPP on the helical grating can be transformed into vortex beams via a ring array. The frequency ranges can be divided into several bands, and the beam-scanning characteristic can be realized in each band. The topological charge (TC) is related to the mode index of the SSPP mode. A physical prototype is fabricated, and the experimental results agree well with the simulation one. The demonstrated vortex beam emitter expands the application of SSPP and provokes several advanced applications.

The helical grating is shown in Fig. 1(a). The width, period, and inner and outer radii are set as $a = 1.5$ mm, $d = 3$ mm, $R_1 = 2$ mm, and $R_2 = 12$ mm. The dispersion properties are investigated primarily by CST STUDIO, as shown in Fig. 1(b) [22]. The dispersion curves of a cylindrical grating with the same structural parameters are also presented by the gray lines. Different from the cylindrical grating, the adjacent dispersion curves of the helical grating exhibit distinct characteristics and the cross emerges at the propagation phase. As a helical structure, the phase of the SSPP varies with the azimuthal angle. The transverse eigen electric field and phase distributions with the phase are shown in Fig. 1(c). The SSPP is confined to the grooves and propagates helically along the grating. The electric field distribution in air is presented and the other half is hidden by the metal in the cross section. As the electric distribution is stronger in air than that on the metal surface, the distribution is consequently asymmetric. The gradient angular phase change indicates that the SSPP carries OAM modes. Generally, the TC "l" is employed to differentiate the OAM mode:

$$l = \pm|m|, \tag{1}$$

where m indicates that the phase changes by $|2m\pi|$ when the angular angle changes by 2π, and the sign $\pm$ indicates that the OAM mode rotates clockwise (+)/counterclockwise (−).

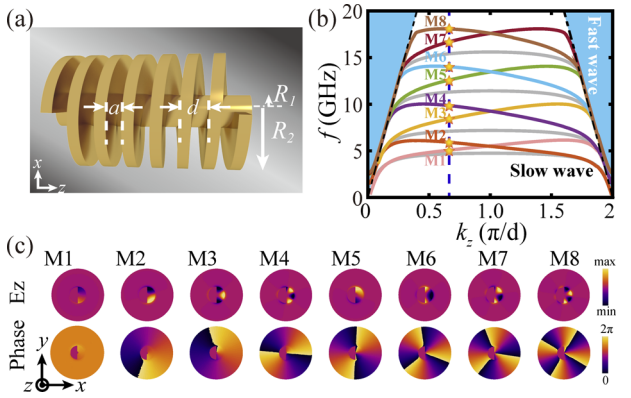

Fig. 1. (a) and (b) Schematic structure and dispersion characteristics of the helical grating. Dispersion curves of the cylindrical grating are marked in gray. Structural parameters are set as $a = 1.5$ mm, $d = 3$ mm, $R_1 = 2$ mm, and $R_2 = 12$ mm. (c) Transverse electric and phase distributions with various modes. The corresponding points are marked in panel (b).

Table 1. TCs of OAM Modes Carried by the SSPP

Index	M1	M2	M3	M4	M5	M6	M7	M8
TC	0	+1	−1	+2	−2	+3	−3	+4

According to the phase variation in Fig. 1(c), l increases with the mode index of the SSPP modes, and is listed in Table 1.

As shown in Fig. 1(b), the wavenumber of the SSPP is larger than that of light, and the SSPP is confined to the grating surface. In this section, the transformation of an SSPP into a vortex beam in the free space is investigated. To change the radiation characteristic, the dispersion curve must be shifted to the fast wave region from the slow wave region in the Brillouin diagram. In this way, an asynchrony ring array is introduced to provide the phase compensation. The emitter is composed of SSPP couplers, helical grating, and ring array, as shown in Fig. 2. The phase compensation is related to the harmonic order and is expressed as $2\pi n/p$, where integer n represents the spatial harmonic order, and p is the period of the ring array. Hence, the wavenumber of the SSPP diffracted by the ring array is revised as

$$k_z = k_{SSPP} + 2\pi n/p, \tag{2}$$

where k_{SSPP} is the wavenumber of the SSPP. Generally, n always has a small absolute value because the power of high-order harmonics is weak enough to be ignored, and the −1st harmonic wave is considered here as it has maximum harmonic intensity [23]. The modulated Brillouin diagram system is shown in Fig. 3(a), and the dispersion curve moves $-2\pi/p$ along the k_z axis compared with the origin curves. Part of the dispersion curve is exposed to the fast wave region, which indicates that the corresponding SSPP wave can be converted to the vortex beam while radiating into the free space. The radiation angle θ is with respect to the propagation and derived based on the wavenumber matching principle as

$$\theta = \arccos(k_z/k_0). \tag{3}$$

Considering the near-field confinement of the SSPP, the electric field intensity exponentially decays along the radial direction. The gap between the ring array and helical grating has a considerable effect on the radiation characteristic. If the gap

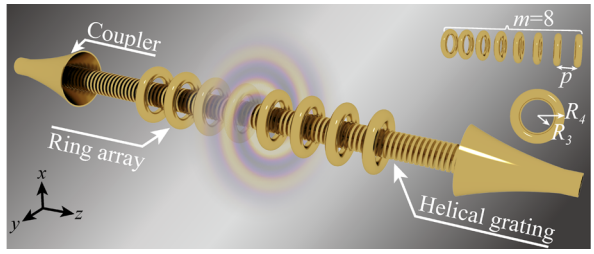

Fig. 2. Schematic model of the vortex beam emitter, where $p = 7$d, $R_3 = 14$ mm, and $R_4 = 12$ mm

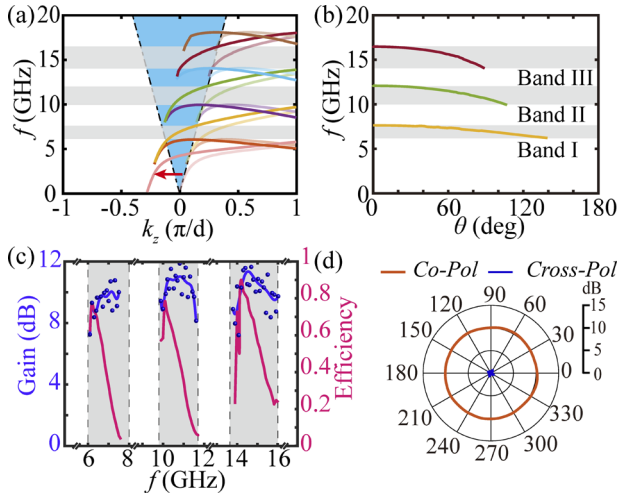

Fig. 3. (a) Brillouin diagram of the compound system. (b) Theoretical radiation direction and (c) directivity gain and efficiency at different frequency bands. (d) Polarization characteristics at 10 GHz.

is narrow, the dispersion properties of the SSPP are inevitably impacted by the ring array, which may lead to multi-frequency radiation owing to the Brillouin-zone folding effect [24]. In this regard, the optimized gap is set as $R_3 - R_2 = 3$ mm. If the diameter is large, the ring acts like a metal wall. Then, the SSPP is suppressed to the surface of the helical grating and cannot efficiently generate radiation. The tiny ring gives rise to a small coupling area, and the radiation effect is weak.

To achieve a high-purity vortex beam, the frequency region with a single dispersion line is employed in this system, as shown in Fig. 3(a), and is marked in shadow regions, as shown in Fig. 3(b). For clarity, the bands are marked as I (6–7.5 GHz), II (9.8–12 GHz), and III (13.7–16.5 GHz). The TCs in these bands are $l = -1$, $l = -2$, and $l = -3$, respectively. The electric distributions on the x-y and y-z planes are presented in Figs. 4(a)–4(c), and the observation areas are 140 mm × 140 mm and 140 mm × 350 mm, respectively. In a conventional vortex beam, the transverse electric intensity presents a hollow distribution, and there is a phase singularity in the center. As the grating is located at the center, the phase singularity is overlapped and is absent. The vortex characteristics can be verified through mode purity. Based on the principle of Fourier transform, the purity of each mode can be obtained as

$$p[l] = (1/2\pi)\int_0^{2\pi} \psi(\varphi) d\varphi \exp(-j\varphi), \tag{4}$$

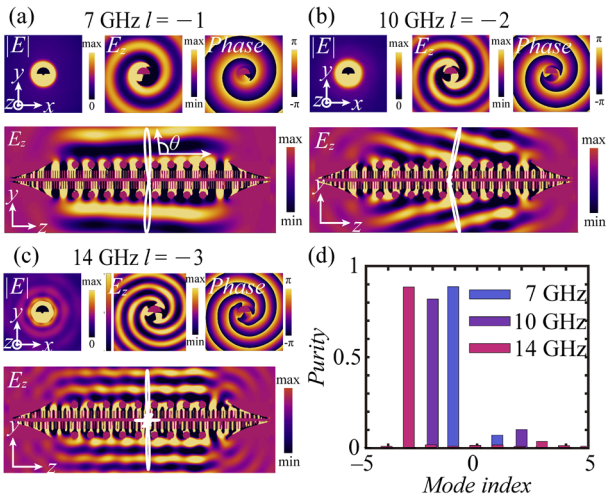

Fig. 4. (a)–(c) Electric distributions and (d) normalized mode purities at different frequencies.

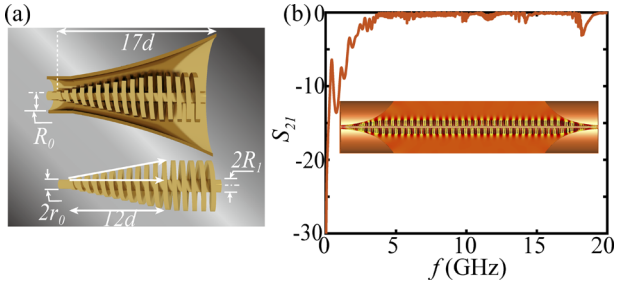

Fig. 5. (a) Schematic design of the coupler, where $r_0 = 1.52$ mm and $R_0 = 3.5$ mm. (b) Transmission properties of the couplers. Inset shows the electric distribution at 10 GHz.

where ψ is the phase distribution and φ represents the azimuthal angle. The calculated data are extracted from a circle with $R = 40$ mm. As shown in Fig. 4(d), the normalized purities are 0.88, 0.82, and 0.89 at 7 GHz, 10 GHz, and 14 GHz, respectively. It shows that this system can generate high-quality vortex beams.

Moreover, the directivity gain and efficiency of the emitter are shown in Fig. 3(c). The maximum directivity gain and efficiency of the emitter are approximately 12 dB and 90% respectively. The efficiency goes through fluctuation and decreases with the increasing working efficiency in each band. This phenomenon is explained as follows. When the working frequency increases, the confinement is enhanced, and the SSPP is tightly confined to the surface as a result. Then the diffraction effect induced by the ring array is weak, and consequently the working efficiency drops. The efficiency can be improved by extending the array length. However, it will increase the fabrication challenge. The optimized ring array is set as $L = 8p$. Additionally, the radiation pattern is omnidirectional with linear polarization. For example, the far-field radiation pattern at 10 GHz is shown in Fig. 4(d). The gain of the co-polarization and cross-polarization is 10 dB and −5 dB, respectively, which implies that the emitter has linear polarization with a low cross-polarization. The co-polarization also shows that the radiation pattern is omnidirectional.

Because of the wavenumber mismatch, the SSPP cannot be excited directly [25–27]. By this means, a coupler is specially designed to bridge the SSPP and the coaxial mode [26]. In this design, a gradient helical grating is employed to achieve high-efficiency conversion between the coaxial mode and the SSPP. The coupler is composed of an outer conductor and an inner grating. The left port is used to connect the vector network analyzer (VNA), and the size is consequently the same as the connecter. The corresponding structural parameters are $r_0 = 1.52$ mm and $R_0 = 3.5$ mm, respectively. The inner and outer radii are increased from r_0 to R_1 and R_2 with a length of $12d$. With the decrease of the outer radius, the dispersion curve is close to the light line, and the mismatch of wavenumber is eliminated [25]. The outer conductor is employed to suppress the electromagnetic wave to achieve an efficient conversion. Meanwhile, it can receive or release the SSPP to improve transmission performance. A pair of couplers are set at both ends of the grating to verify the transmission properties, and the result is shown in Fig. 5(b). The transmission property is poor in the low-frequency range and near 0 dB from 3 GHz to 18 GHz. Additionally, the energy leakage in the low-frequency range may be caused by the diffraction of fast-wave components in high-order mode and can be ignored as the working frequency band is 6–16.5 GHz. It is worth noting that there are several fluctuations in the transmission curves. The phenomenon is explained by the dispersion curves. When near the asymptotic frequency, the group velocity approaches zero, and part of the energy fails to transmit to the receiving port. The problem can be eliminated by extending the calculation times. In addition, the electric distribution at 10 GHz is presented in the inset of Fig. 5(b).

For experimental verification, the helical grating is fabricated via high-precision 3D metal printing technology, and the machining tolerance is at the 0.1-mm level. The fabrication material is stainless steel GH3625. To reduce the metal loss, the fabricated prototype is polished and coated with copper by electroless plating. The coupler is made of oxygen-free copper, and the ring array is made of aluminum to reduce the weight. To facilitate assembly, two fixed holes are drilled symmetrically. In addition, spacers that are made of aluminum tubes are used to keep the uniform distribution of ring elements. Moreover, two fixed rods are designed to assemble the ring array with the helical grating, and the fabricated vortex beam emitter is shown in Fig. 6(a). It is pointed out that fixed rods have less impact on the generation of vortex beams via simulation verification.

In the experimental setup, one port of the emitter is connected to the VNA, and the other port is connected to a matching component. The beam-scanning functions are primarily verified. The experimental setup is shown in Fig. 6(b), and the probed result is shown in Fig. 6(c). The theoretical result is also presented with the dotted white line. The experimental results agree well with the theoretical ones in various bands. There are also other radiation modes in the radiation intensity distribution. It is explained that other SSPP modes are converted into spatial radiation. Despite this, the beam-scanning function of the emitter is less impacted. The fabrication error may cause the dispersion curves of the high-order mode to shift from the theoretical one, giving rise to small deviations between the measured and simulation results. Then, the vortex property is experimentally proved. As the electric distribution cannot be detected directly, the angular phase distributions at 7 GHz, 10 GHz, and 14 GHz are measured and presented in Figs. 6(d)–6(f). The phase decreases by 2π, 4π, and 6π in the angular direction, which indicates the TCs are −1, −2, and −3, respectively. There are excellent agreements between the experimental and simulation results. In this way, both the beam-scanning and vortex functions are verified.

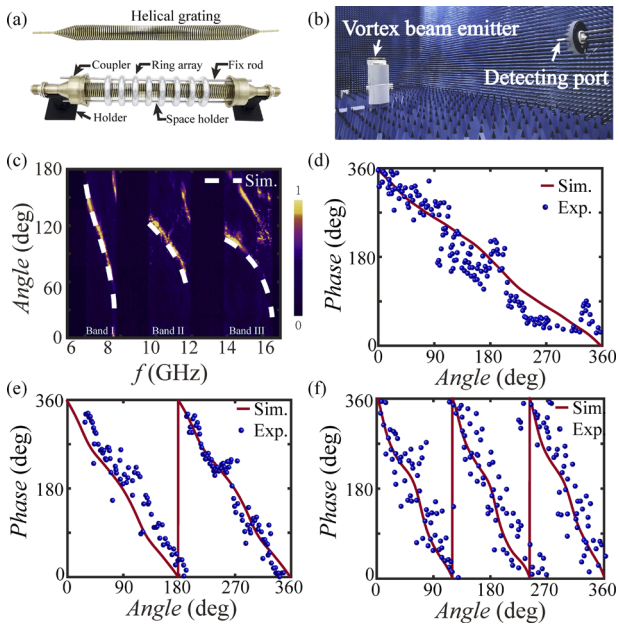

Fig. 6. (a) and (b) Pictures of the fabricated vortex beam emitter and experimental setup. (c) Radiation intensity distribution. The normalized experimental result is presented by the pseudocolor map, and the simulation result is marked with the white dotted line. (d)–(f) Angular phase distributions at 7 GHz, 10 GHz, and 14 GHz.

The proposed vortex beam emitter shows several advantages. Compared with emitters based on the resonant SSPP antenna, the bandwidth is widely extended, and the radiation direction can be tuned flexibly [15,16]. The structure is also much simpler and more robust than the free-electron-driven vortex emitter [17,18]. The electric-optic system for focusing the electron beam is removed. Additionally, this emitter may find numerous applications in communication systems. The multi-mode vortex beam can be used to multiplex the signal. The beam-scanning may find applications in point-to-point communication, and the radiation pattern can also be converted into directional radiation via a parabolic surface.

In summary, a multi-mode vortex beam emitter based on the SSPP is demonstrated in this Letter. The SSPP on the helical grating is used to convert into the high-purity vortex beam via a ring array in several frequency ranges, and the TC varies with the radiation band. Frequency-controlled beam scanning is achieved in each band. A physical prototype is fabricated, and the experiment agrees well with the simulation. This multi-mode vortex beam emitter is compact and promising for OAM-based communication systems.

Funding. National Natural Science Foundation of China (NSAF U1830201); National Key Research and Development Program of China (2021YFA1600302); Beijing Science Foundation for Distinguished Young Scholars (JQ21011); Newton Advanced Fellowship of Royal Society of London (NAF\R1\180121).

Disclosures. The authors declare no conflicts of interest.

Data availability. Data underlying the results presented in this paper are not publicly available at this time but may be obtained from the authors upon reasonable request.

REFERENCES

1. R. A. Beth, Phys. Rev. **50**, 115 (1936).
2. J. Wang, J.-Y. Yang, I. M. Fazal, N. Ahmed, Y. Yan, H. Huang, Y. Ren, Y. Yue, S. Dolinar, M. Tur Alan, and E. Willner, Nat. Photonics **6**, 488 (2012).
3. M. Padgett and R. Bowman, Nat. Photonics **5**, 343 (2011).
4. R. Fickler, R. Lapkiewicz, W. N. Plick, M. Krenn, C. Schaeff, S. Ramelow, and A. Zeilinger, Science **338**, 640 (2012).
5. K. Huang, P. Shi, G. Cao, K. Li, X. Zhang, and Y. Li, Opt. Lett. **36**, 888 (2011).
6. J. T. Barreiro, T. C. Wei, and P. G. Kwiat, Nat. Phys. **4**, 282 (2008).
7. E. Brasselet, M. Malinauskas, A. Žukauskas, and S. Juodkazis, Applied Physics Letter **97**, 211108 (2010).
8. R. C. Devlin, A. Ambrosio, N. A. Rubin, J. B. Mueller, and F. Capasso, Science **358**, 896 (2017).
9. S. M. Mohammadi, L. K. S. Daldorff, J. E. S. Bergman, R. L. Karlsson, B. Thide, K. Forozesh, T. D. Carozzi, and B. Isham, IEEE Trans. Antennas Propag. **58**, 565 (2010).
10. S. X. Yu, L. Li, G. M. Shi, C. Zhu, X. X. Zhou, and Y. Shi, Appl. Phys. Lett. **108**, 121903 (2016).
11. J. C. Xu, L. H. Chen, X. J. Zhai, T. Zhang, L. Mcdonald-Maier, S. G. Huang, and K. Be, Eng. Sci. **10**, 51 (2020).
12. J. B. Pendry, L. Martín-Moreno, and F. J. Garcia-Vidal, Science **305**, 847 (2004).
13. X. Shen, T. J. Cui, D. Martin-Cano, and F. J. Garcia-Vidal, Proc. Natl. Acad. Sci. U. S. A. **110**, 40 (2013).
14. F. J. Garcia-Vidal, A. I. Fernández-Domínguez, L. Martin-Moreno, H. C. Zhang, W. X. Tang, R. W. Peng, and T. J. Cui, Rev. Mod. Phys. **94**, 025004 (2022).
15. Z. Liao, N. Z. Jia, G. Q. Luo, M. Wang, S. Sun, T. Zhou, H. F. Ma, T. J. Cui, and Y. M. Liu, Phys. Rev. Appl. **13**, 054013 (2020).
16. J. Y. Yin, J. Ren, L. Zhang, H. J. Li, and T. J. Cui, Laser Photonics Rev. **12**, 1600316 (2018).
17. J.-F. Zahu, C.-H. Du, Z.-W. Zhang, P.-K. Liu, L. Zhang, and A. W. Cross, Opt. Lett. **46**, 4682 (2021).
18. Z. W. Zhang, C. H. Du, J. F. Zhu, F. Y. Han, F. H. Li, Z. C. Gao, L. Zhang, A. W. Cross, and P. K. Liu, J. Lightwave Technol. **39**, 6231 (2021).
19. J. F. Zhu, C. H. Du, W. E. I. Sha, Z. W. Zhang, and P. K. Liu, IEEE Antennas Wirel. Propag. Lett. **20**, 2290 (2021).
20. A. I. Fernández-Domínguez, C. R. Williams, F. J. García-Vidal, L. Martín-Moreno, S. R. Andrews, and S. A. Maier, Appl. Phys. Lett. **93**, 141109 (2008).
21. F. Rüting, A. Fernández-Domínguez, L. Martín-Moreno, and F. García-Vidal, Phys. Rev. B **86**, 075437 (2012).
22. CST, "CST PS Tutorial," https://www.3ds.com/zh/products-services/simulia/products/cst-studio-suite/.
23. L. Z. Yin, F. Y. Han, J. Zhao, Y. D. Wang, D. Wang, T. J. Huang, and P. K. Liu, IEEE Antennas Wirel. Propag. Lett. **20**, 1215 (2021).
24. J. F. Zhu, C. H. Du, T. J. Huang, L. Y. Bao, and P. K. Liu, Opt. Express **27**, 26192 (2019).
25. D. W. Zhang, Y. X. Sun, K. Zhang, Q. Wu, and T. Jiang, Opt. Lett. **46**, 4354 (2021).
26. D. W. Zhang, X. Liu, Y. X. Sun, K. Zhang, Q. Wu, Y. S. Li, and T. Jiang, J. Phys. D: Appl. Phys. **55**, 165101 (2022).
27. H. H. Tang, T. J. Ma, and P. K. Liu, Appl. Phys. Lett. **108**, 191903 (2016).